



ELSEVIER

Available online at www.sciencedirect.com

SCIENCE @ DIRECT®

Earth and Planetary Science Letters 214 (2003) 575–588

EPSL

www.elsevier.com/locate/epsl

High resolution image of the subducted Pacific (?) plate beneath central Alaska, 50–150 km depth

Aaron Ferris^{a,*}, Geoffrey A. Abers^a, Douglas H. Christensen^b,
Elizabeth Veenstra^b

^a Boston University, Department of Earth Sciences, 685 Commonwealth Ave, Boston, MA 02215, USA

^b University of Alaska Fairbanks, Geophysical Institute, 903 Koyukuk Dr., Fairbanks, AK 99775, USA

Received 3 March 2003; received in revised form 1 July 2003; accepted 10 July 2003

Abstract

A receiver function transect across the Alaska Range images the subducting Pacific plate at 50–150 km depth. Across a 200 km long array of 30 receivers, the largest observed P-to-S conversions come from the top of the subducting slab. This signal is coherent across the array and is strongly asymmetric, requiring a complicated interface at the top of the slab. Waveform inversion shows that the conversion is generated by a 11–22 km thick low velocity zone at the top of the slab, as much as 20% slower than the surrounding mantle. The velocity of this zone increases with increasing depth of the slab, approaching velocities of the mantle near 150 km depth. All intermediate depth earthquakes occur within the zone, along a plane dipping 5° steeper. The layer is too thick to represent metamorphosed oceanic crust, as proposed for other subduction zones. It may represent a thick serpentinized zone or, more likely, a thick exotic terrane subducting along with the Pacific plate.

© 2003 Elsevier B.V. All rights reserved.

Keywords: receiver function; serpentinite; Yakutat; Wadati–Benioff zone

1. Introduction

Buoyancy suggests that crustal sections thinner than 15 km should subduct while those thicker than 20 km should not [1]. With increasing depth, crustal buoyancy should reverse as subducted crust metamorphoses to eclogite [2]. In principle this is testable through observation of the thick-

ness and velocities of subducted crust, because gabbroic crust remains seismically distinct from mantle rocks until it converts to eclogite [3]. However, subducted crust presents a small target and has been difficult to image. Recently, several unusual earthquake signals have been attributed to subducting oceanic crust [4,5], revealing a 2–10 km thick zone at the top of the subducting plate with velocities 5–15% slower than the surroundings [4,5]. While these observations generally confirm the presence of an un-equilibrated (i.e. not yet eclogitized) oceanic crust to at least 150 km depth, they provide little indication of the range of thicknesses that might subduct, and the

* Corresponding author. Tel.: +1-617-358-1078;

Fax: +1-617-353-3290.

E-mail address: aferris@bu.edu (A. Ferris).

observing methods provide only weak constraints on the depths of eclogitization.

Teleseismic converted phases permit a direct method to image slab structure, and they have been used to image layering in slabs beneath central Oregon and the central Andes. Beneath Cascadia a prominent low velocity layer is observed to 45 km depth and is interpreted as hydrated subducted crust [6,7]. Presumably the low velocities do not extend deep because the slab is hot; likewise, slab seismicity is absent. In the Andes, beneath a region of highly thickened crust, a slab low velocity zone (LVZ) is imaged in patches to 120 km depth where it disappears [8]. Seismicity also ceases at this depth, and it is thought that the oceanic crust has completely metamorphosed to eclogite.

We use teleseismic P-to-S converted phases to image a transect across the plate subducting beneath central Alaska (Fig. 1). Here, seismicity extends to 120–150 km depth, and the upper plate is near 35–40 km thick. The most prominent feature in the transect is a signal from the slab between 60 and 150 km depth. Waveform inversion indicates that the signal represents a thick LVZ at the top of the slab, which increases in velocity with increasing slab depth. The LVZ is unexpectedly thick, suggesting subduction of an exotic terrane rather than just the Pacific plate. It metamorphoses to similar wavespeeds as its surroundings at 120–140 km depth, near the deepest seismicity.

2. Tectonic setting

The Aleutian subduction system terminates at the Gulf of Alaska. The subducting plate here has an unusually shallow dip at depths less than 50 km, leading to one of the widest interplate thrust zones anywhere [9]. Only in this part of the Aleutian system are mountains being built, and a volcanic arc is absent [10]. All of these characteristics are shared by other regions of flat-slab subduction [11] and may reflect the subduction of unusually buoyant lithosphere.

East of Mount McKinley the strike of the Wadati–Benioff zone (WBZ) changes orientation (Fig. 1), possibly indicating a tear or segmenta-

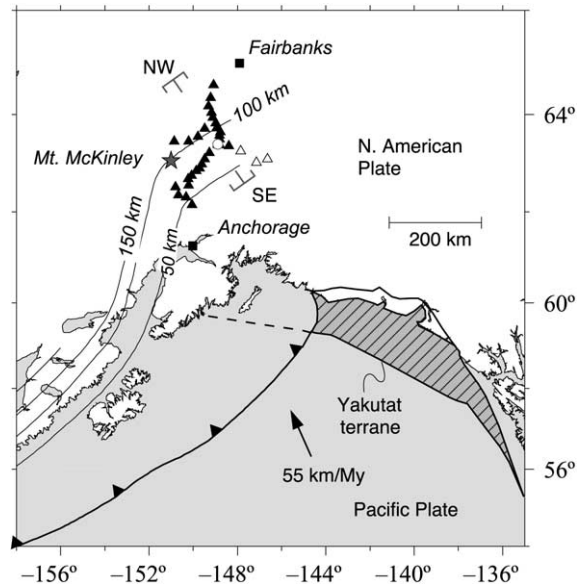


Fig. 1. Map of central Alaska showing BEAAR station locations (black triangles); open triangles are stations omitted from analysis because they are beyond the end of the slab. Brackets show the receiver function transect in Figs. 2, 3, 7–10; white circle is the zero coordinate in all cross-sections. Barbed line delineates the Aleutian trench. Thin solid lines are depth contours of intermediate depth seismicity. Hatched region is the boundary of Yakutat terrane (modified from [17]). Dashed line marks a magnetic anomaly inferred to be the southwestern extent of subducted Yakutat terrane [18].

tion in the subducting plate [12]; the WBZ also shallows eastward. Most earthquakes are <150 km deep. Tomography reveals P-wave velocity anomalies 3–6% faster in the slab than the surrounding mantle with slow mantle velocities in the overlying mantle wedge [13], similar to other subduction zones [14].

Alaska is one of the few places undergoing active accretion of exotic terranes, a process that has continued since the Mesozoic [10]. At the Earth's surface, the Yakutat terrane presently impinges on the North American continent (Fig. 1). The terrane began colliding with North America in the early Miocene [10]. GPS measurements indicate that the Yakutat block presently moves at 44 mm/yr to the northwest relative to North America [15], so that the terrane is kinematically part of the Pacific plate. The western two-thirds may be underlain by oceanic basement, and the westernmost portion has been recently subducted

entirely beneath the Aleutian megathrust, removing much of the overlying accretionary prism in the process [16]. Offshore seismic reflection and refraction data show that the Yakutat terrane is a largely mafic layer which lies over the Pacific plate, separated by a few km of low velocity material, for an overall thickness of ~ 15 km including the underlying Pacific oceanic crust [17]. A prominent magnetic anomaly, inferred to be the subducted continuation of the western limit, extends at least 200 km west from the Aleutian trench (dashed line in Fig. 1 [18]), indicating the up-dip limit of the Yakutat terrane extends from 138°W to 150°W . The down-dip end remains unknown, although the data presented below indicate that it may extend to at least 150 km depth.

3. Data and methods

3.1. Experiment

Seismograms were collected during the Broad-band Experiment across the Alaska Range (BEAAR), a 2.5 year IRIS/PASSCAL experiment ending in August 2001. A network of 36 broadband seismographs were deployed above the subducting Pacific plate where the WBZ lies between 50 km and 150 km depth (Fig. 1). Twenty-eight stations were aligned at ~ 10 km spacing, north to south, while eight stations were aligned east to west. Between June and September 2000 all 36 stations operated, after which 17 stations continued until August 2001. Seven stations operated for an additional year in 1999–2000. The network design provides crossing rays from teleseisms at depths greater than 30 km and provides correlated waveforms for teleseismic signals sampling subcrustal structure. Data were continuously re-

corded at 50 samples per second and timing was corrected to within 1 ms via GPS. The Gurlap CMG3T and CMG3ESP sensors provide a flat velocity response between 0.05 and 120 or 30 s periods. All data collected are archived at the IRIS Data Management Center.

3.2. Receiver functions

Receiver functions yield estimates of the P-to-S converted arrivals generated at interfaces below a seismic station [19,20]. Our receiver calculation employs a time domain deconvolution between single event–station pairs [21,22]. Before deconvolution the data are decimated to 6.25 Hz and windowed to contain 40 s of signal and 6 s of pre-signal noise. After deconvolution a 0.6 Hz Gaussian low pass filter removes high frequency noise, and the records for each station are stacked over all events at a common back-azimuth range.

Beneath the BEAAR network, teleseismic signals arriving from the northwest intersect the slab perpendicular to strike in the up-dip direction, an orientation for which the incident wavefield produces strong P-to-S conversions off the dipping slab [23]. Because the up-dip signals maximize the conversion amplitudes and are unaffected by out-of-plane ray bending, we limit analysis to signals from four well-recorded, western Asian earthquakes with back-azimuths of $302\text{--}350^\circ$ (Table 1). Earthquake signals from the southeast also arrive perpendicular to the slab strike, hence we examine signals from five Central American earthquakes (Table 2). Numerous teleseisms at other back-azimuths (e.g. $200\text{--}300^\circ$) show effects from the slab but arrive obliquely to slab strike, so can be affected by slab geometry in complicated ways and are not included in the simple analysis presented here.

Table 1
Events from western Asia used to calculate receiver functions

Origin time	Latitude ($^\circ$)	Longitude ($^\circ$)	Depth (km)	Back-azimuth ($^\circ$)	Distance ($^\circ$)
6/06/2000 2:41:49	40.69	32.99	10	350	76
6/07/2000 21:46:55	26.86	97.24	33	302	75
7/17/2000 22:53:47	36.28	70.92	141	330	75
12/06/2000 17:11:06	39.57	54.80	30	341	76

To produce an interpretable image of the upper mantle we back-project the receiver functions to their nominal P-to-S conversion depths [24,25], using an iasp91-like velocity model [26]. This calculation assumes P-to-S conversions from horizontal interfaces, so converted phases arriving from dipping layers (i.e. the slab) appear slightly shallower than the actual interfaces. For the slab geometry imaged here, this apparent dip effect images the slab 1–3 km shallower than would full migration. The waveforms are then projected to a transect at 330° azimuth, perpendicular to the slab strike mapped by [10] (Fig. 1). Stations close to the center of this line project to points < 5 km apart, more near the ends of the transect. Lastly, we take advantage of the redundancy offered by the close signal spacing and average nearby records with a Gaussian spatial smoothing function similar to [27] (Fig. 2). Smoothing emphasizes coherent energy from nearby stations while minimizing effects of scattering and noise. The half-width of the Gaussian function is 10 km, so that stations within a 10 km radius of a stacking point dominate the stack.

4. Receiver function transect

The receiver function transect provides a 250 km long coherent image of the upper mantle to 200 km depth (Figs. 2 and 3). Its most striking feature is a high amplitude arrival between 60 and 150 km depth, increasing in depth to the northwest, which we interpret as a P-to-S conversion from the top of the subducting plate. This signal is quite large, usually the largest on the record, and it correlates well in location with WBZ earthquakes. The increasing depth of this phase to the

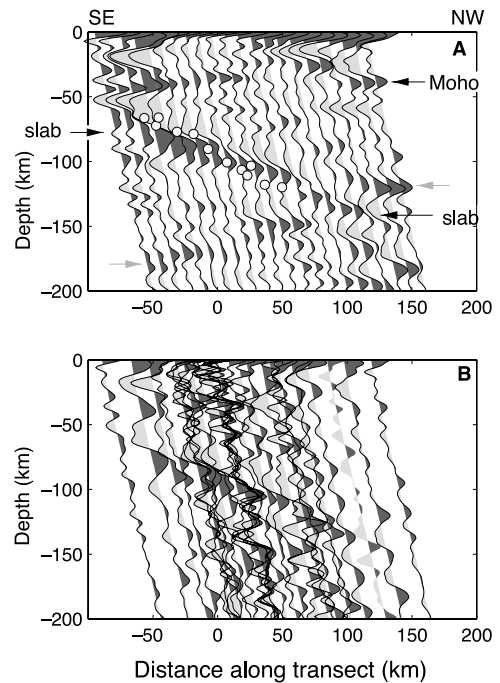


Fig. 2. Receiver function transect using signals from four teleseismic earthquakes from western Asia ($\sim 330^\circ$ back-azimuth; Table 1). Panels A and B represent two different levels of processing (see Section 3.2). (A) Spatially smoothed receiver function image generated from the data shown in the bottom figure. The direct slab and Moho P-to-S signals are labeled, including the main Moho reverberation (gray arrow). (B) Receiver function stacks for each station. Data are low pass filtered (0.6 Hz), projected to the station positions along the transect line, and back-ray projected to P-to-S conversion depths. Teleseismic signals from this back-azimuth intersect the slab perpendicular to strike in the up-dip direction, producing the strong slab signal seen between 60 and 150 km depth. Black are positive amplitude arrivals and gray are negative amplitude arrivals. Intermediate depth earthquakes are shown for reference. See Fig. 1 for transect line location.

Table 2
Events from Central America used to calculate receiver functions

Origin time	Latitude (°)	Longitude (°)	Depth (km)	Back-azimuth (°)	Distance (°)
9/30/1999 16:31:15	16.06	-96.93	61	118	59
9/09/2000 11:41:47	18.20	-102.48	46	123	55
1/13/2001 17:33:32	13.05	-88.66	60	111	65
4/29/2001 21:26:54	18.74	-104.55	10	125	54
5/20/2001 4:21:43	18.18	-104.45	33	125	54

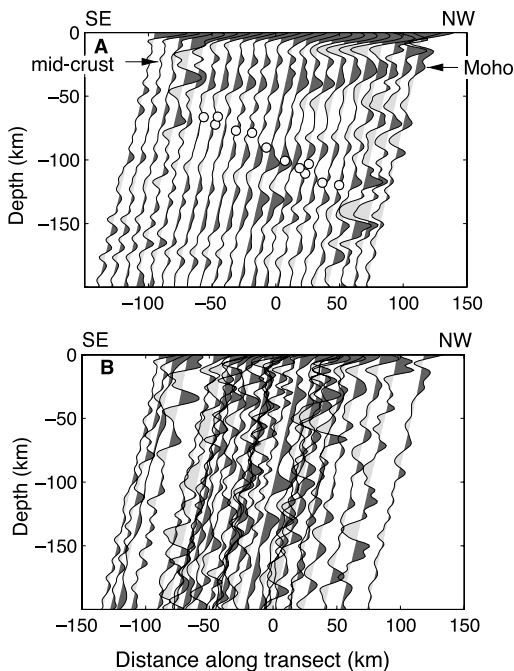


Fig. 3. Receiver function transect using signals from five events in Central America ($\sim 120^\circ$ back-azimuth; Table 2). Processing and layout are the same as in Fig. 2. (A) Spatially smoothed receiver function transect. (B) Individual station stacks. Teleseismic signals from this back-azimuth are incident normal to slab dip and, hence, do not produce an apparent slab signal. Crustal phases are labeled (black arrows).

northwest and its absence from the Central American signals reinforce its interpretation as a conversion from a northwest dipping interface or interfaces (Fig. 2). Ray theory predicts that signals from the southeast should generate small slab conversions due to their near normal incidence angle with the slab [23] (Fig. 3).

Both images (Figs. 2 and 3) show P-to-S conversion between 34 and 46 km depth, shallowing to the northwest, interpreted as continental Moho [28]. Crustal P-to-S arrivals are clearer in signals arriving from the southeast and include a mid-crustal phase near 20 km depth. Coherent Moho arrivals fade near the center of the transect in Fig. 2, possibly from scattering off topography at the base of the crust. From both back-azimuths a near horizontal arrival appears at 125–150 km depth, modeled as the first arriving Moho reverberation (Figs. 2 and 3). It may interfere with the

slab P-to-S signal around 150 km depth in the northeast section of the transect (Fig. 2). Negative polarity arrivals within the upper 50 km indicate additional crustal structure, but tests discussed below show that they do not significantly alter the slab pulse.

We observe two important properties of the slab conversion. First, the signal exhibits strong asymmetry: a negative polarity arrival precedes the dominant positive polarity arrival. A negative polarity P-to-S conversion requires a velocity inversion, indicating that an LVZ lies at the top of the slab. The raw data exhibit this asymmetry as does the smoothed image, and the asymmetry is seen when signals are low passed at 0.2 Hz (not shown), indicating it is a robust feature. Second, both positive and negative peaks are significantly broader than the Moho P-to-S conversion, an observation that requires a bound on the LVZ structure. Specifically, it requires the LVZ to be thick compared to the quarter-wavelength of these signals.

Numerical simulations demonstrate that increasing the velocity contrast between the LVZ and the surrounding mantle increases the amplitude of both P-to-S conversions, while increasing the LVZ thickness broadens the signal [23]. With synthetic receiver functions we examine several possible LVZ models and their effect on slab signal asymmetry, varying the thickness of the zone, the velocity gradient on its boundary, and the velocity contrast between the LVZ and the surrounding mantle (Fig. 4). These tests indicate that the observed signal requires either a constant velocity LVZ (Fig. 4a) or an LVZ with a sharp boundary at its base and a gradient at the top (Fig. 4d). To understand how crustal complexity affects the overall signal we also analyze other models that include a gradient on the Moho, mid-crustal layers or a near surface low velocity layer. A thin surface layer (0.5–2.0 km thick) is the only complexity needed to explain the negative polarity arrivals at < 5 s. Such a layer does not cause obvious interference with the slab signals (Fig. 4b). Although non-unique, these tests suggest that the LVZ has sharp boundaries, particularly at its base, and its signal is not systematically affected by upper plate structure.

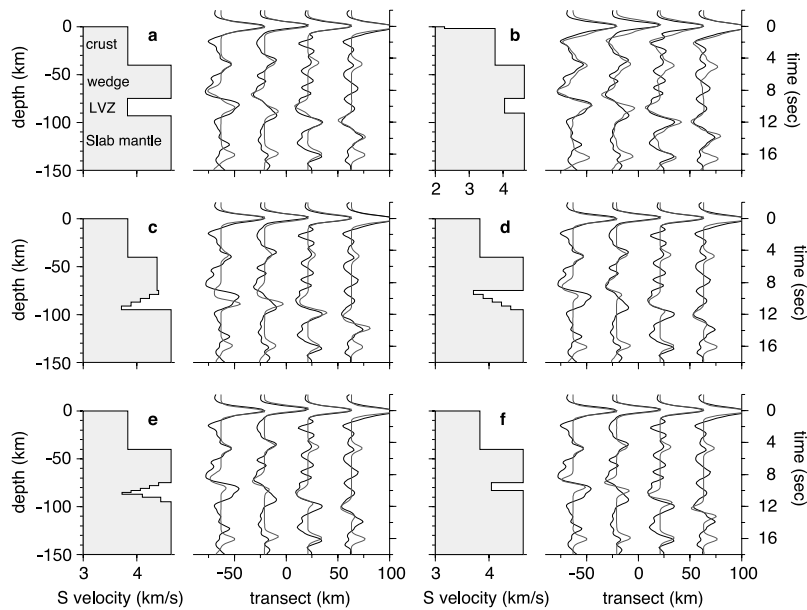


Fig. 4. Numerical simulations comparing six simple slab LVZ structures to select receiver functions. Synthetic receiver functions are calculated assuming a slab dipping at 25° and a ray incidence angle perpendicular to slab strike. Velocity models used to generate the synthetic waveforms are plotted to the left of the waveforms. Synthetics (thin gray lines) are aligned with the slab arrivals by varying the slab depth. Data are plotted with heavy black lines. The different LVZ models are: (a) a 15 km thick LVZ with a constant Poisson ratio, (b) a similar model as in (a), except with a 2 km thick, near surface layer, explaining most of the negative polarity energy in the first few seconds of the record, (c) an LVZ with a gradient at both boundaries, (d) an LVZ with a sharp boundary at its base and a gradient at its top, (e) an LVZ with a sharp boundary at the top and a gradient at its base, (f) a thin LVZ representative of oceanic crust. Only models a, b and c produce slab signals similar those seen in the data.

Several alternative mechanisms for producing a broad slab signal can be ruled out. (1) The spatial smoothing filter cannot provide the broadening, because the pulse width does not vary with the filter used. (2) Crustal conversions do not vary across the array in the same direction as the slab signal, hence, it is unlikely that crustal multiples are constructively interfering with slab signals to generate broadening or negative polarity arrivals. This includes a signal from near surface layers (see above; Fig. 4b). (3) It is conceivable that complicated crustal structure could act as a low pass filter on the slab signal, widening it with respect to the crustal conversions. However, we experimented with models of a number of complex structures across both the Moho and the midcrust and were unable to reproduce the pulse broadening. (4) Attenuation could remove high frequencies from the slab signal. However, at frequencies between 0.1 and 1.0 Hz the slab pulse is always broader than the crustal conversions, sug-

gesting that the frequency dependent effects are not significant. Also, any attenuation effects should increase to the northwest, where slab signals sample thicker more attenuative lithosphere [29], but the pulse does not broaden down-dip. (5) Complicated refraction effects along the dipping slab might influence the converted signal width. However, numerical simulations with both ray based and full waveform calculations (not shown) could not produce these effects. In conclusion, the slab arrival is generated by an LVZ between slab and wedge mantle. The broadness of the signal is a consequence of the thickness of this velocity inversion zone. In order to explain these features the LVZ needs to be significantly slower than the surrounding mantle and relatively thick.

5. Waveform inversion

The asymmetry of the slab signal becomes pro-

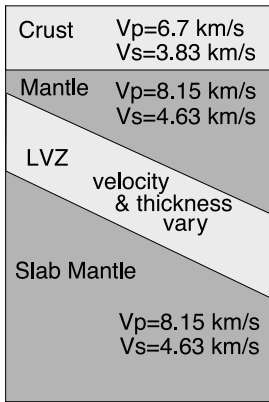


Fig. 5. Velocity model used in the waveform inversion (see Section 5).

gressively less pronounced as depth increases, implying that the LVZ anomaly reduces with slab depth. To quantify this relationship, we invert a portion of each waveform for parameters describing the LVZ as a homogeneous, dipping layer (Fig. 5). The inversion estimates three parameters: LVZ thickness, velocity, and depth of the LVZ. It does so independently at each transect point by fitting the observed to calculated waveforms. Full synthetic waveforms are generated assuming a LVZ dipping at 25° to the NNW, at a nominal depth of 80 km beneath a 35 km thick flat lying crust, using a ray based procedure [19]. The inversion fits the data around a ~ 6 s window encompassing the slab signal low and high pulses, although complete waveforms are calculated. This parameterization simplifies the actual slab structure, but it should allow a robust description of the variation of the LVZ with depth.

The inversion determines LVZ layer thickness and P velocity (V_p), via a grid search for the rms misfit between the time windowed slab signals and the synthetics. We estimate the third parameter, LVZ depth, from the cross-correlation of the slab signal to the synthetics at each step in the grid search. The depth is that of the slab P-to-S conversion point at the top of the slab, accounting for slab ray bending. Because interferences do not complicate the slab signals and mantle wedge velocity varies little, the phase isolation method we use for fitting parameters will give results equivalent to full waveform fitting. Prior to fitting,

both the data and synthetics are low pass filtered at 0.4 Hz, the highest frequency at which results are stable. Confidence limits in the LVZ parameters are shown at 95%, based on a F -test of the misfit variance in the grid search [30]. For the F -test we estimate 1.0 degree of freedom per second of data following [31].

We test two suites of LVZ models, each with a different constraint on the Poisson ratio (ν) of the LVZ, to constrain the S velocity (V_s) from V_p . The first suite mimics the transition from a dry harzburgite ($\nu=0.26$) to a serpentinized harzburgite ($\nu=0.38$; HS model in Fig. 6). The second inversion assumes a constant ν of 0.26 (CP model; Fig. 6). These represent endmembers of possible ways in which V_p and V_s could be related. Velocities of the endmembers are mixed with Hashin–Shtrikman averaging [32]. Endmember compositions and velocities are from [33], calculated at 2.5 GPa and 700°C . In all grid searches the P velocity varies between 5.5 and 8.15 km/s, and the LVZ thickness varies between 0 and 40 km at 1 km intervals.

5.1. Inversion results

We invert a total of 16 waveforms along the

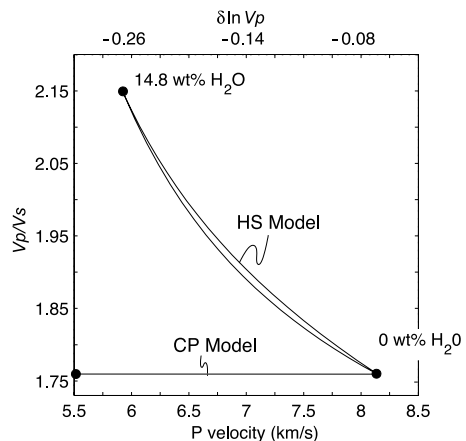


Fig. 6. The relationship between V_p/V_s and P velocity of the LVZ, used to generate the suite of synthetics for the waveform inversion. The HS model represents the mixing between a harzburgite and a serpentinized harzburgite, assuming 2.5 GPa and 700°C . The CP model has a constant V_p/V_s value of 1.76. See text for definition of $\delta \ln V_p$ values.

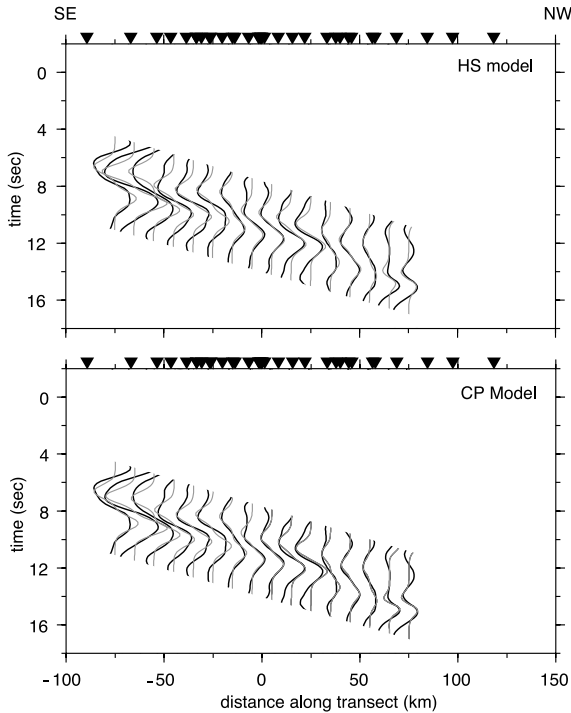


Fig. 7. Synthetic waveform fits for the HS model (top) and CP model (bottom). Only the slab phase is shown. Dark lines are the observed data and the gray lines are best fit synthetics. Black triangles are station positions along the transect.

transect (Figs. 7–10). All show clear slab signals from stations between $x = 50$ and $x = 150$ km (horizontal axis in Fig. 7), the densest sampled portion of the transect. Two waveforms from the north-west end of the transect ($x = 140$ km and $x = 150$ km) may contain interference from Moho multiples, but elsewhere signals from upper plate structure do not obviously affect the slab arrivals (see Section 4). Signals generated by a near surface layer (Fig. 4b) do not systematically interfere with the slab signal or alter the rms misfit in the inversion.

Both models fit the data well: the global misfit variance normalized to the power in the data of the HS model is 0.112 and of the CP model is 0.191, a difference of 6% which is not statistically significant even at 90% confidence. In both sets of inversions the LVZ velocity increases with increasing slab depth, becoming indistinct from surrounding mantle velocities near 150 km depth.

Between 70 and 150 km depth, the HS model shows $\delta \ln V_p$ (fractional P-wave velocity anomaly in the waveguide) increasing from -0.26 ± 0.05 to -0.05 ± 0.01 (Fig. 8). Our velocity model does not take into account long wavelength variations due to thermal structure, so we report waveguide velocities as $\delta \ln V_p = (V_p - V_{p \text{ ref}}) / V_{p \text{ ref}}$, where $V_{p \text{ ref}}$ (8.15 km/s) is the background mantle velocity, rather than V_p directly. The results in the CP model give an equivalent increase, $\delta \ln V_p = -0.34 \pm 0.09$ at 70 km depth increasing to -0.07 ± 0.02 at 150 km depth (Fig. 9). The average uncertainties in $\delta \ln V_p$ are ± 0.04 for the HS model and ± 0.07 for the CP model, while uncertainties in $\delta \ln V_s$ are both near ± 0.05 . The difference in uncertainties can be understood from the receiver functions' greater sensitivity to V_s [34] and the non-linear relationship between V_p and V_s in the HS model (Fig. 6).

The LVZ has a relatively constant thickness along the transect. The mean thickness in the HS model is 15 km with average uncertainties of 5 km, and measurements range between 6 and 20 km (Figs. 8 and 10). In the CP model the mean thickness is 16 km (Fig. 9). Thickness is mostly constrained by the broadness of the slab signal (see Section 4) and shows no trend with depth. These results require that the LVZ be sig-

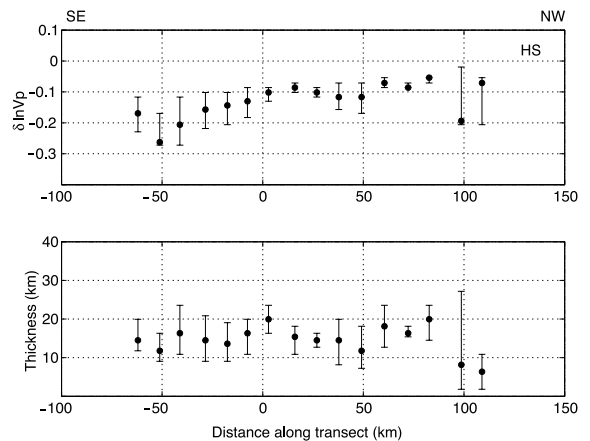


Fig. 8. LVZ parameters from the waveform inversion for the HS model. Results are corrected for ray bending using the velocity model in Fig. 5. (Top) LVZ $\delta \ln V_p$ and 95% uncertainty bounds. (Bottom) LVZ thickness and 95% uncertainty bounds. See Section 5.1 for a definition of $\delta \ln V_p$ values.

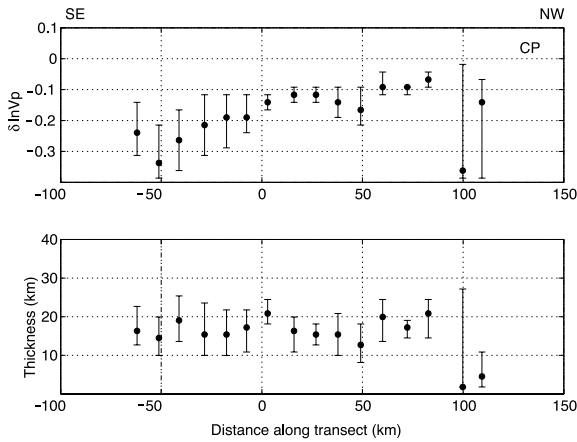


Fig. 9. LVZ parameters from the waveform inversion for the CP model. Format is the same as in Fig. 8.

nificantly thicker than oceanic crust, unlike estimates of LVZ for other subduction zones [5,8].

The inversions gives a slab dip of 22° from 65 to 153 km depth with depth uncertainties of ±2.5 km. The depth to the top of the LVZ depends on the velocity of the overlying mantle wedge, and at

least two effects may slightly bias these results. First, it has been shown that mantle velocities are slower above deeper portions of the slab in Alaska [13], which is typical for many mantle wedges [14]. Low wedge velocities are also suggested by low Q [29]. The effect of a 5% variation in wedge velocity, the maximum commonly observed in many wedges, would yield a ~2° shallower slab dip with our calculation. Second, our transect may not be exactly perpendicular to slab strike, hence true slab dip might be steeper. Slab strike defined by [10] is roughly 030°, however some seismicity studies show it near 040° [12]. Also, the mean back-azimuth range of our signals is 331°, varying by ±21°. If the maximum discrepancy between the down-dip direction and event back-azimuth is 25°, our dip calculation would steepen by 2°. These systematic biases suggest that our estimation of slab dip might be off by 2°, in either direction.

The LVZ boundaries from the inversion results differ slightly in depth from the amplitude peaks in the back-projected receiver functions (Fig. 10).

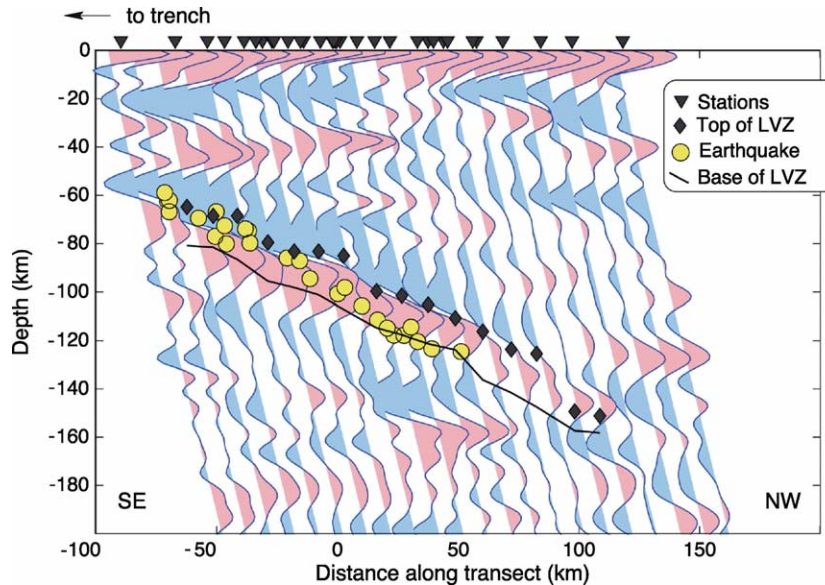


Fig. 10. Waveform inversion results compared to the receiver function transect. Black diamonds represent the top of the LVZ determined from the waveform inversion for the dipping slab model. The black line is the base of the LVZ. Both are corrected for ray bending from a 025° dipping interface. Circles are intermediate depth earthquakes located in the same velocity model as used in the LVZ inversion. Receiver functions are plotted in the same manner as Fig. 2. The back-projection used to plot the waveforms does not account for ray bending due to the layer dip, which results in a slight discrepancy between the peaks of the slab negative and positive pulses and the LVZ boundaries (see text).

This apparent disparity reflects two simplifications in the back-projection method used to plot the waveforms, simplifications that allow objective imaging at all depths. First, the projection does not account for ray bending due to the slab dip, so the negative polarity arrivals appear shifted upwards. The waveform inversion shows that the top of the slab (diamonds in Fig. 10) is 1–3 km deeper than negative polarity peaks. Second, the projection does not account for slab low velocities, increasing the apparent depth of the base of the LVZ. Finally, applying a low pass filter to the data slightly distorts the apparent width of the LVZ in the waveforms.

6. Discussion

Our results indicate the presence of an LVZ atop the subducting plate between 60 km and 150 km depth. Throughout this depth range the LVZ remains seismically distinct from the surrounding mantle, suggesting that it has not fully equilibrated to eclogite [3]. This observation is consistent with what has been observed in several other arcs [4,5], although most previous studies do not resolve the depth variation in velocity seen here. Low velocity layers appear to be a common but not ubiquitous features at the tops of subducting plates.

6.1. WBZ earthquakes and the LVZ

Our estimate of LVZ depth is independent of earthquake locations, so allows the position of the WBZ to be determined relative to the slab structure. In order to examine the relationship of the LVZ to the WBZ, we relocate 121 intermediate depth events, using direct P and S arrival times from the BEAAR network and the Alaska Earthquake Information Center (AEIC) network. The events occur during three months in 2000 when all BEAAR stations operated. Hypocenters are determined in the same 1-D velocity model as that used in the receiver function analysis (Fig. 6) to minimize systematic biases (see Section 5.1). We exclude phase arrivals at stations >150 km from the epicenter to limit potential effects of long

ray paths along the slab [35], although their inclusion yields similar results. Also, events less than 50 km deep or greater than 50 km from the transect line are excluded.

The relocated earthquakes delineate a thin band that lies within the LVZ but dips at a 5° steeper angle (Fig. 8). Earthquakes vary from the top of the LVZ near 65 km depth to its base at 120 km depth. Deeper earthquakes were not recorded by BEAAR. Relocation of 10 years of AEIC data [12] shows occasional seismicity extends to 150 km depth, in a zone dipping steeper than our LVZ, but most deeper events lie west of the BEAAR main transect. These deeper earthquakes may represent a different slab segment [12], or may occur below the LVZ. The BEAAR based locations also lie in a narrower band than the previous relocations, with less than 5 km scatter about a surface compared to 10–20 km scatter from other data [12], presumably reflecting the greatly increased station density and use of S arrivals.

These observations can be understood in the context of physical models for intermediate depth earthquakes. At the high confining pressures of these events, frictional sliding is possible only if some unusual process facilitates failure [36]. The release of H₂O through dehydration reactions may in some way embrittle rock [36–38], an interference supported by correlation between seismicity and the predicted depth range for dehydration [39]. In Alaska, earthquakes occur only within the LVZ, as expected if the LVZ is a dehydrating layer and earthquakes are triggered by dehydration. Hence, the earthquakes lie only within the LVZ because that is where dehydration takes place. The decay in velocity anomaly with increasing depth resembles what one would expect from gradual dehydration of this layer, as does the decay in seismicity. It is not clear why earthquakes step deeper within the LVZ with increasing depth; possibly, they define a critical reaction boundary or a low permeability channel. It is conceivable that some other process unrelated to fluids is localizing the earthquakes within the LVZ, but the pattern of intermediate depth seismicity suggests that the presence of the LVZ is critical to seismogenesis.

6.2. The nature of the LVZ

Any explanation for the LVZ in Alaska must satisfy four main observations: (1) the LVZ thickness is between 11 and 22 km, (2) its thickness does not change with depth, (3) its velocity increases with depth but is slower than surrounding mantle even at 150 km depth, and (4) intermediate depth earthquakes occur only within it. In other subduction zones LVZs have been imaged and are explained as dehydrating oceanic crust. At least six circum-Pacific arcs show LVZs that are 2–8 km thick at ≥ 100 km depth from high frequency wave dispersion [5], including a nearby region in Alaska [40]. It is possible that these studies image only a thin layer due the high frequencies they sample (0.5–8.0 Hz), while the 0.01–0.4 Hz band used here is sensitive to broader features. However, after several numerical simulations we have been unable to find a single structure that could simultaneously reproduce both kinds of observations. In other subduction zones, receiver function studies also reveal thin LVZs, including a 5–10 km thick LVZ at 120 km depth beneath the Andes [8], and a ~ 6 km thick LVZ at 75 km depth beneath Cascadia [41]. Beneath northeastern Japan, P-to-S converted phases from local earthquakes show a 5–10 km thick layer with a 6–12% velocity anomaly, thought to represent subducted oceanic crust [42]. Hence, the observations presented here appear to be unusual; the LVZ thickness is at least twice that normally observed for oceanic crust [43,44].

Dehydration of subducting slabs can lead to serpentinization of overlying mantle wedge, provided temperatures remain low in some region [45]. Serpentinization can also occur in the slab mantle from the introduction of fluids at mid-ocean ridge fracture zones, or seaward of the trench by normal faulting [46]. Because isotherms lie generally subparallel to the slab, either scenario could lead to a thick layer of serpentinite paralleling it. The slow velocities are consistent with a moderate degree of serpentinization (Fig. 6). For most mafic and ultramafic rocks stable at > 2.5 GPa (the depths of interest), each 1 wt% H₂O corresponds to a 2% decrease in P velocity [47]. Hence, if serpentinization produces the LVZ

velocities, then the LVZ should have $10 \pm 5\%$ wt% H₂O at 65 km depth, decreasing to $3 \pm 2\%$ wt% H₂O at 125 km depth (Fig. 8). Such a decrease in water content could correspond to some form of gradual serpentine breakdown, or a more complex sequence of dehydration reactions involving loss of serpentine and chlorite, as predicted for several subduction zones [39].

However, it is difficult to understand why a thick serpentinite layer would be observed beneath Alaska and not beneath other arcs. There is no obvious reason why the Alaska slab would be unusually hydrated. The downgoing plate lies in the middle of the range of thermal parameters observed for slabs globally [48], so thermal structure should be similar to many subduction zones previously sampled. The shallow part of the slab (< 50 km depth) has unusually low dip which should affect temperatures at shallow depths [11], but it is not clear how this enhances mineral stability deeper.

Alaska is also unusual in that it is one of the few places globally undergoing active terrane accretion, and it is possible that the thick layer observed here represents a subducting terrane. As discussed in Section 2, the Yakutat terrane may be subducting at shallow depths. The LVZ thickness measured here, 11–22 km, resembles the overall thickness of ~ 15 km for the Yakutat terrane and underlying Pacific crust seen in marine refraction studies [17]. If the inferred southern boundary of the Yakutat terrane (dashed line in Fig. 1) is extrapolated in the direction of plate convergence, then the down-dip extent of this terrane would lie near Mt. McKinley at 100 km depth. In other words, the Yakutat terrane might underlie the BEAAR stations on top of the subducting slab.

Several implications emerge from the inference that the Yakutat terrane subducts with the Pacific plate to 150 km depth. First, the terrane must be ~ 500 km long in the down-dip direction. At current plate velocities (55 mm/yr [49]), that would require Yakutat subduction for at least the last 9 Myr, consistent with geological constraints on the timing of collision [10]. Second, the differences between the LVZ imaged here and that seen from body wave dispersion [40] can be explained by the

differences in sampling area. The ray paths sampled by the dispersion study all lie southwest of Mt. McKinley, down-dip from where normal Pacific plate subducts, while the BEAAR receiver functions sample the slab farther to the east. Third, the 15 km thickness observed here lies just under the thickness limit predicted from buoyancy [1], so should be buoyant but subductable. Fourth, the presumed thick crust also lies down-dip of where the Pacific Plate assumes an unusually shallow dip at 0–50 km depth. Perhaps, the buoyancy of the subducting crust provides a driving force for slab flattening, driving mountain building and perhaps shutting off magmatism. Finally, the Alaska example may provide one of the best examples on Earth of subduction of thick crust, the sort of setting presumed to be responsible for formation of many ultra-high pressure metamorphic rocks now observed on the surface.

7. Conclusion

Beneath central Alaska, a high density receiver function transect reveals strong signals from the subducting Pacific plate (Fig. 10). On many receiver functions the slab signal is the largest on the record, particularly for up-dip rays that intersect the slab at high incidence angles. The signals show characteristics of a conversion from a dipping layer, but are too large (and asymmetric) to be explained as a simple discontinuity. Instead, both forward modeling and inversion require a LVZ atop the subducting plate between 60 and 150 km depth. The LVZ is 11–22 km thick and up to 20% slower than the surrounding mantle, with a velocity anomaly that decays with increasing depth.

The velocities and their pattern of decay resemble that expected for a thick dehydrating layer at the top of the subducting plate. The inferred thickness is greater than that of subducted crust, and greater than that observed with a variety of techniques in other settings. Possibly, the slab signal illuminates a thick serpentized zone either above or below the subducting crust (or both). However, the unusual characteristics of this zone and its relationship to the accretionary tectonics

of southern Alaska suggest an alternative. Perhaps, the unusually thick layer being imaged here is a subducting exotic terrane, such as the Yakutat terrane. The imaged Yakutat terrane offshore has a similar overall thickness and its western extent lies directly up-dip (in the direction of plate motion) from the area sampled here. If so, the image here may be one of the few direct pieces of evidence that thickened crust can subduct, at least to the 50–150 km depths at which many ultra-high pressure metamorphic rocks form.

This idea is clearly speculative, but should be testable. One test would be to extend the BEAAR transect up-dip, to test for structural continuity with structures imaged offshore. Another would be to directly compare signals in BEAAR with ones obtained along strike. Even if this interpretation is incorrect, the image observed here is one of the clearest images of a subducting slab attained to date, and shows that the slab remains distinct from surrounding mantle to at least 150 km depth.

Acknowledgements

This research was supported by NSF Grant EAR-9996451. Instruments and technical assistance were provided through the IRIS PASSCAL Instrument Center. Field work was made possible only through help from J. Stachnik, B. Scott, D. Hoak, A. Holland, C. Beebe, and S. Pozgay. We would also like to thank M. Templeton for her expertise in data management, E. Silver for making us think about the Yakutat block, D. Zhao, two anonymous reviewers, and the editor S. King for helpful suggestions that strengthened the final manuscript. Many of the figures were prepared using GMT software [50]./SK/

References

- [1] P. Molnar, D. Gray, Subduction of continental lithosphere; some constraints and uncertainties, *Geology* 7 (1979) 58–62.
- [2] W.D. Pennington, Role of shallow phase changes in the subduction of oceanic crust, *Science* 220 (1983) 1045–1047.

- [3] D. Gubbins, A. Barnicoat, J. Cann, Seismological constraints on the gabbro-eclogite transition in subducted oceanic crust, *Earth Planet. Sci. Lett.* 122 (1994) 89–101.
- [4] G.R. Helffrich, Subducted lithospheric slab velocity structure; observations and mineralogical inferences, in: G.E. Bebout, D.W. Scholl, S.H. Kirby, J.P. Platt (Eds.), *Subduction Top to Bottom*, American Geophysical Union, 1996, pp. 215–222.
- [5] G.A. Abers, Hydrated subducted crust at 100–250 km depth, *Earth Planet. Sci. Lett.* 176 (2000) 323–330.
- [6] S. Rondenay, M.G. Bostock, J. Shragge, Multiparameter two-dimensional inversion of scattered teleseismic body waves; 3, application to the Cascadia 1993 data set, *J. Geophys. Res.* 106 (2001) 30,795–30,807.
- [7] M.G. Bostock, R.D. Hyndman, S. Rondenay, S.M. Peacock, An inverted continental Moho and serpentinization of the forearc mantle, *Nature* 417 (2002) 536–538.
- [8] X. Yuan, S.V. Sobolev, R. Kind, O. Oncken, G. Bock, G. Asch, B. Schurr, F. Graeber, A. Rudloff, W. Hanka, K. Wylegalla, R. Tibi, C. Haberland, A. Rietbrock, P. Giese, P. Wigger, P. Rower, G. Zandt, S. Beck, T. Wallace, M. Pardo, D. Comte, Subduction and collision processes in the Central Andes constrained by converted seismic phases, *Nature* 408 (2000) 958–961.
- [9] J.M. Davies, L. House, Aleutian subduction zone seismicity, volcano-trench separation, and their relation to great thrust-type earthquakes, *J. Geophys. Res.* 84 (1979) 4583–4591.
- [10] G. Plafker, J.C. Moore, G.R. Winkler, Geology of the southern Alaska margin, in: G. Plafker, H.C. Berg (Eds.), *The Geology of Alaska*, v. G1, Geological Society of America, Boulder, CO, 1994, pp. 389–449.
- [11] M.A. Gutscher, S.M. Peacock, Thermal models of flat subduction and the rupture of great subduction zone earthquakes, *J. Geophys. Res.* 108 (2003) 10.1029/2001JB000787.
- [12] N.A. Ratchkovski, R.A. Hansen, New constraints on tectonics of interior Alaska; earthquake locations, source mechanisms, and stress regime, *Bull. Seismol. Soc. Am.* 92 (2002) 998–1014.
- [13] D. Zhao, D. Christensen, H. Pulpan, Tomographic imaging of the Alaska subduction zone, *J. Geophys. Res.* 100 (1995) 6487–6504.
- [14] D. Zhao, Seismological structure of subduction zones and its implications for arc magmatism, *Phys. Earth Planet. Inter.* 127 (2001) 197–214.
- [15] H.J. Fletcher, J.T. Freymueller, New GPS constraints on the motion of the Yakutat Block, *Geophys. Res. Lett.* 26 (1999) 3029–3032.
- [16] J. Fruehn, R. von Huene, M.A. Fisher, Accretion in the wake of terrane collision; the Neogene accretionary wedge off Kenai Peninsula, Alaska, *Tectonics* 18 (1999) 263–277.
- [17] T.M. Brocher, G.S. Fuis, M.A. Fisher, G. Plafker, M.J. Moses, J.J. Taber, N.I. Christensen, Mapping the megathrusts beneath the northern Gulf of Alaska using wide-angle seismic data, *J. Geophys. Res.* 99 (1994) 11,663–11,686.
- [18] T.R. Bruns, Model for the origin of the Yakutat Block, an accreting terrane in the northern Gulf of Alaska, *Geology* 11 (1983) 718–721.
- [19] C.A. Langston, Modeling crustal structure through the use of converted phases in teleseismic body-wave forms, *Bull. Seismol. Soc. Am.* 67 (1977) 677–691.
- [20] K.G. Dueker, A.F. Sheehan, Mantle discontinuity structure from midpoint stacks of converted P to S waves across the Yellowstone hotspot track, *J. Geophys. Res.* 102 (1997) 8313–8327.
- [21] A.F. Sheehan, G.A. Abers, C.H. Jones, A.L. Lerner-Lam, Crustal thickness variations across the Colorado Rocky Mountains from teleseismic receiver functions, *J. Geophys. Res.* 100 (1995) 20,391–20,404.
- [22] G.A. Abers, X. Hu, L.R. Sykes, Source scaling of earthquakes in the Shumagin region, Alaska; time-domain inversions of regional waveforms, *Geophys. J. Int.* 123 (1995) 41–58.
- [23] J.F. Cassidy, Numerical experiments in broadband receiver function analysis, *Bull. Seismol. Soc. Am.* 82 (1992) 1453–1474.
- [24] C.H. Jones, R.A. Phinney, Seismic structure of the lithosphere from teleseismic converted arrivals observed at small arrays in the southern Sierra Nevada and vicinity, California, *J. Geophys. Res.* 103 (1998) 10,065–10,090.
- [25] H. Kao, G. Rui, R.-J. Rau, S. Danian, R.-Y. Chen, G. Ye, F.T. Wu, Seismic image of the Tarim Basin and its collision with Tibet, *Geology* 29 (2001) 575–578.
- [26] K.L.N. Kennett, E.R. Engdahl, R. Buland, Constraints on seismic velocities in the Earth from traveltimes, *Geophys. J. Int.* 122 (1995) 108–124.
- [27] S.L. Neal, G.L. Pavlis, Imaging P-to-S conversions with multichannel receiver functions, *Geophys. Res. Lett.* 26 (1999) 2581–2584.
- [28] E.V. Meyers-Smith, D.H. Christensen, G.A. Abers, Moho topography beneath the Alaska Range: Results from BEAAR, *EOS Trans. AGU 83 Fall Meet. Suppl.* (2002) S52A–1073.
- [29] J.C. Stachnik, E.V. Meyers-Smith, D.H. Christensen, G.A. Abers, Mantle wedge temperature estimates and implications for wedge melting from seismic attenuation, *EOS Trans. AGU 83 Fall Meet. Suppl.* (2002) S52A–1069.
- [30] P.G. Silver, W.W. Chan, Shear wave splitting and subcontinental mantle deformation, *J. Geophys. Res.* 96 (1991) 16,429–16,454.
- [31] X. Yang, K.M. Fischer, G.A. Abers, Seismic anisotropy beneath the Shumagin Islands segment of the Aleutian-Alaska subduction zone, *J. Geophys. Res.* 100 (1995) 18,165–18,177.
- [32] J.P. Watt, G.F. Davies, R.J. O’Connell, The elastic properties of composite minerals, *Rev. Geophys. Space Phys.* 14 (1976) 541–563.
- [33] B.R. Hacker, G.A. Abers, S.M. Peacock, Subduction factory 1: Theoretical mineralogy, density, seismic wave-

- speeds, and H₂O content, *J. Geophys. Res.* 108 (2003) 10.1029/2001JB001127.
- [34] C.J. Ammon, The isolation of receiver effects from teleseismic P waveforms, *Bull. Seismol. Soc. Am.* 81 (1991) 2,504–2,510.
- [35] J.P. McLaren, C. Frohlich, Model calculations of regional network locations for earthquakes in subduction zones, *Bull. Seismol. Soc. Am.* 75 (1985) 397–413.
- [36] S.H. Kirby, E.R. Engdahl, R.P. Denlinger, Intermediate-depth intraslab earthquakes and arc volcanism as physical expressions of crustal and uppermost mantle metamorphism in subducting slabs, in: G.E. Bebout, D.W. Scholl, S.H. Kirby, J.P. Platt (Eds.), *Subduction Top to Bottom*, American Geophysical Union, 1996, pp. 195–214.
- [37] C. Meade, R. Jeanloz, Deep-focus earthquakes and recycling of water into the Earth's mantle, *Science* 252 (1991) 68–72.
- [38] C.B. Raleigh, Tectonic implications of serpentinite weakening, *Geophys. J. R. Astron. Soc.* 14 (1967) 113–118.
- [39] B.R. Hacker, S.M. Peacock, G.A. Abers, Subduction factory 2: Are intermediate-depth earthquakes in subduction zone slab linked to metamorphic dehydration reactions? *J. Geophys. Res.* 108 (2003) 10.1029/2001JB001129.
- [40] G.A. Abers, G. Sarker, Dispersion of regional body waves at 100–150 km depth beneath Alaska; in situ constraints on metamorphism of subducted crust, *Geophys. Res. Lett.* 23 (1996) 1171–1174.
- [41] J.F. Cassidy, R.M. Ellis, S wave velocity structure of the northern Cascadia subduction zone, *J. Geophys. Res.* 98 (1993) 4407–4421.
- [42] T. Matsuzawa, N. Umino, A. Hasegawa, A. Takagi, Upper mantle velocity structure estimated from PS-converted waves beneath the northeastern Japan arc, *Geophys. J. R. Astron. Soc.* 86 (1986) 767–787.
- [43] R.S. White, D. McKenzie, R.K. O'Nions, Oceanic crustal thickness from seismic measurements and rare earth element inversions, *J. Geophys. Res.* 97 (1992) 19,683–19,715.
- [44] C.Z. Mutter, J.C. Mutter, Variations in thickness of layer 3 dominate oceanic crustal structure, *Earth Planet. Sci. Lett.* 117 (1993) 295–317.
- [45] S.M. Peacock, Numerical simulation of metamorphic pressure-temperature-time paths and fluid production in subducting slabs, *Tectonics* 9 (1990) 1197–1211.
- [46] S.M. Peacock, Are the lower planes of double seismic zones caused by serpentine dehydration in subducting oceanic mantle?, *Geology* 29 (2001) 299–302.
- [47] G.A. Abers, T. Plank, B.R. Hacker, The wet Nicaraguan slab, *Geophys. Res. Lett.* 30 (2003) 10.1029/2002GL015649.
- [48] A. Gorbatov, V. Kostoglodov, Maximum depth of seismicity and thermal parameter of the subducting slab; general empirical relation and its application, *Tectonophysics* 277 (1997) 165–187.
- [49] C. DeMets, R. Gordon, D. Argus, S. Stein, Current plate motions, *Geophys. J. Int.* 101 (1990) 425–478.
- [50] P. Wessel, W.H.F. Smith, Free software helps map and display data, *EOS Trans. AGU* 72 (1991) 441, 445–446.